Fully Discrete VO_2 Particulate Film with Ultra-High Transmittance and Excellent Thermochromic Performance

Bin Li[1], Shouqin Tian[,1], Longxiao Zhou[1], Senwei Wu[1], Tingfeng Ma[1], Guanjie He[2, 3], Baoshun Liu[1] and Xiujian Zhao*[,1]*

[1]State Key Laboratory of Silicate Materials for Architectures, Wuhan University of Technology (WUT), No. 122, Luoshi Road, Wuhan 430070, P. R. China

[2]Christopher Ingold Laboratory, Department of Chemistry, University College London, London WC1H 0AJ (UK)

[3]Electrochemical Innovation Lab, Department of Chemical Engineering, University College London, London WC1E 7JE (UK)

*Corresponding authors; E-mail: tiansq@whut.edu.cn, opluse@whut.edu.cn

ABSTRACT

VO_2 has attracted widespread attention due to its extraordinary thermochromic properties. Visually transparent VO_2 films hold great promise for applying in smart windows, smart radiative coolers, solar cells and microwave absorbing windows. However, it remains a huge challenge to simultaneously achieve the ultra-high luminous transmittance (T_{lum}) and excellent thermochromic performance due to their contradictory relationship. Here, we develop a fully discrete VO_2 particulate (FDVP) film with an ultra-high T_{lum} of 92.7% achieved by significantly reducing reflectance. It is highly transparent to near infrared (NIR) light below the phase transition temperature (T_c, 69.1 ºC), but blocks NIR light above T_c through the strong localized surface plasmon resonance (LSPR) effect, resulting in an excellent solar energy modulation (ΔT_{sol}) of 10.5% for smart windows. In addition, a 3.5at.%W doped FDVP film exhibits a desired T_c of 25.8 ºC, an extremely narrow hysteresis width (ΔT) of 4.6 ºC, and good optical properties (T_{lum}=92.0%, ΔT_{sol}=8.2%). The performance represents a new milestone for thermochromic VO_2 films. This work will shed light on the structural design for high performance VO_2 films.

Keywords: vanadium dioxide; particulate film; thermochromic performance; transparent; phase transition temperature; solution method

1. Introduction

Vanadium dioxide (VO_2) has been a research hotspot for the past few decades.[1] It exhibits a rapid and fully reversible semiconductor-to-metal (STM) transition at 68 ºC, accompanied by a structural transition from monoclinic (VO_2(M)) to rutile (VO_2(R)) phase.[2] The accompanied dramatic changes in optical transmittance, resistance, and emissivity across the STM transition have given rise to diverse applications for VO_2, including smart windows, smart radiative coolers,[3-7] infrared camouflage,[8,9] microwave absorbers,[10] electrical switches,[11,12] and thermally activated actuators.[12,13]

The structures of VO_2 are usually designed to maximize their thermochromic performance. At the same time, it is essential to endow some specific applications with visually transparent feature to make full use of the sunlight spectrum.[3] The visually transparent VO_2 is essential for various devices, such as traditional smart windows that block near-infrared light;[13-16] radiation coolers for smart windows[3,4] and solar cells;[4] and microwave absorbing windows for communications, medical and aerospace equipment.[10] The common demands for those applications are that the ultra-high T_{lum} across the SMT transition need to maintained and the difference in NIR transmittance (ΔT_{sol}), mid infrared emissivity ($\Delta\varepsilon$) and microwave absorption ($\Delta\alpha$) are as large as possible. However, the strong absorption of VO_2(M) and reflectance of VO_2(R)[15,17] in the visible light region give rise to the contradictory relationship between T_{lum} and thermochromic performance (ΔT_{sol}, $\Delta\varepsilon$, and $\Delta\alpha$),[13,16,18] considering the fact that thermochromic performance is positively related to the VO_2 content while T_{lum} is negatively related to the VO_2 content.[3,4,16] For instance, increasing the VO_2 film thickness in the smart windows generally improves ΔT_{sol},

but T_{lum} is decreased. This causes tremendous difficulties in developing highly transparent VO_2 films with excellent ΔT_{sol}.[16,17,19] In addition, the concept of visually transparent VO_2-based smart windows with passive radiative cooling regulation has recently been proposed.[3] A very low T_{lum} of 27.8% and excellent $\Delta\varepsilon$ of 0.4 were obtained by a VO_2 film composed of dispersed VO_2 nanoparticles (VO_2 NPs) and poly(methyl methacrylate). Moreover, T_{lum} can be improved to 62% in another radiative cooling device, where the VO_2 metasurface layer with VO_2 coverage of about 50% was designed. However, $\Delta\varepsilon$ was only 0.26 because of the content of VO_2 in the device was significantly decreased.[4]

Nevertheless, much efforts have been devoted to develop the highly transparent VO_2 films, especially in the wide-studied smart windows application.[17] VO_2 NPs film with ultra-high T_{lum} of 93.3% was designed by Lu *et al*.,[16] while ΔT_{sol} was only 6.1%. In addition, surface patterning, a strategy to construct a typical 'porous structure' with periodic VO_2 domains on the glass surface, has emerged to improve the optical properties.[15,20,21] Typically, Liu *et al*.[15] fabricated an ultra-transparent VO_2 coating composed of ordered VO_2 honeycomb structure *via* a dual-phase transformation. Although, the maximum visible transmittance of 95.4% at 700 nm was achieved, but a mediocre ΔT_{sol} of 5.5% was obtained. It is worth noting that the currently prepared highly transparent VO_2 films always presented very poor ΔT_{sol} (<10%), and which to the best of our knowledge has not been addressed yet. Although, VO_2 films exhibit different thermochromic performances in different applications, the construction of discontinuous VO_2 structure, i.e, dispersed NPs or metamaterials, is a universal strategy to achieve the visually transparent property.[4,10,11,15,16,22,23] On the one hand, the discontinuous VO_2 structure can effectively increase T_{lum} by reducing the effective refractive index (n_{eff}).[16,18] On the other hand, the surface plasmonic resonance

response in VO_2(R) over a broad spectral range from visible to mid-infrared will enhance $\Delta\varepsilon$ and ΔT_{sol} by increasing the light absorption.[3,4,16,24]

Here, we propose the VO_2 films with ultra-high T_{lum} and excellent thermochromic performance. The films are deposited on both sides of the glass *via* a novel template-free solution method (**Figure 1**a). By regulating the porosity of the VO_2 films (or the dispersion of the VO_2 NPs), the optical properties of the VO_2 films are flexibly optimized. A FDVP film consisting of uniformly distributed and fully discrete VO_2 NPs shows the highest porosity of 58.3%, it thus delivers ultra-high T_{lum} of up to 92.7%. Importantly, it is highly transparent in NIR region in the semiconducting state below T_c (69.1 ºC), but blocks NIR light in the metallic state above T_c. Thus, a superior ΔT_{sol} of 10.5% for smart windows is obtained. The ultra-high T_{lum} is attributed to the high porosity and small particle size. The enhanced NIR absorption induced by the localized surface plasmonic resonance (LSPR) in VO_2(R) NPs is responsible for the superior ΔT_{sol}, since no LSPR effect is observed in VO_2(M) NPs. Moreover, the high T_c and ΔT of the VO_2 film, which hinders its practical application, should also be addressed simultaneously.[7-12] Thus, a 3.5at.%W doped FDVP film is also prepared and presents outstanding performance with T_c of 25.8 ºC, ΔT of 4.6 ºC, T_{lum} of 92.1% and ΔT_{sol} of 8.2%.

2. Results and Discussion

2.1 Compositions and Structures of the FDVP Film

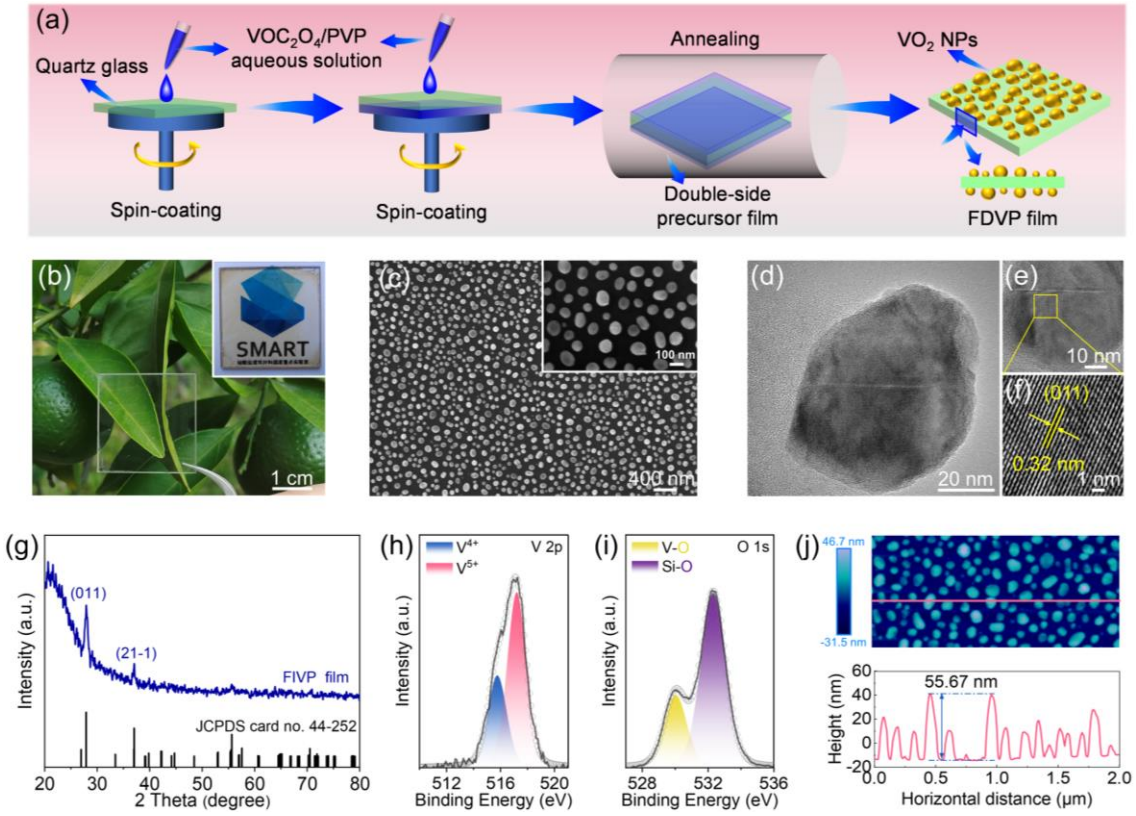

Figure 1 a) Schematic illustration of the synthesis route for the FDVP film. b) Photographs of the ultra-transparent FDVP film (sample S3), the inset shows that the FDVP film exhibits a very light tan color. c) SEM images of the FDVP film. d-f) TEM images of the VO_2 NPs scraped from the FDVP film. g) XRD pattern of the FDVP film. High resolution XPS results for h) V 2p and i) O 1s of the FDVP film, the results are calibrated by the standard C 1s binding energy of 284.8 eV. j) AFM image of the FDVP film and the corresponding height signal from the section (pink line) in the AFM image.

Figure 1b shows the photograph of the FDVP film (sample S3), which is ultra-transparent and exhibits a very light tan color. Its ultra-high transparency is also demonstrated by the fact that the photograph taken from the film-covered lens is almost as clear as those normally taken (**Figure S1**). The SEM images (**Figure 1**c) show that the FDVP film consists of fully discrete VO_2 NPs with a diameter of less than 100 nm. Notably, the structures of the FDVP film on both sides of the substrate are considered to be the same, as the same conditions are used in the fabrication process. TEM images (**Figure 1**d,f) of the VO_2 NPs indicate that the NPs have high crystallinity. And the (011) plane with interplanar spacing of 0.32 nm is clearly observed, which means the crystal is VO_2(M). In the XRD pattern (**Figure 1**g) of the FDVP film, diffraction peaks at 2θ of 27.9° and 37° match well with the standard diffraction peaks of (011) and $(21\bar{1})$ planes in VO_2(M) (JCPDS card no.44-0252, space group: *P*21/c, *a*=5.75 Å, *b*=4.53 Å, *c*=5.38 Å, and β=122.60°). Accordingly, TEM, XRD and Raman results (**Figure S2**) confirm the successful preparation of VO_2(M) film. The XPS results obtained from the film surface are presented in **Figure 1**g,h. The peaks located at 515.8, 517.3, 530.1 and 532.4 eV are indexed to V^{4+}, V^{5+}, O^{2-} in VO_2(M) (O_{V-O}) and O^{2-} in quartz glass (O_{Si-O}), respectively.[22,25] The existence of V^{5+} is attributed to the oxidation of the NPs surface.[26] The rather strong peak for O_{Si-O} indicates that the high porosity in the film, leading to the detection of signals from the quartz glass substrate,[25] which is consistent with the SEM results. The typical structure of fully discrete VO_2 NPs is further investigated by AFM. As shown in **Figure 1**j, the VO_2 NPs are isolated by air, and the maximum height for individual VO_2 NPs is determined to be about 55 nm by the section of the AFM image.

The microstructures of the obtained VO_2 films are flexibly tunable by adjusting the concentration of VO^{2+} and the thickness of precursor film. For convenience, the VO_2 films prepared by changing the thickness of VOC_2O_4-PVP precursor film are labelled in **Table S1**, sample S3 is the FDVP film. The porosity increased with the decrease of the thickness of precursor film from samples S1 to S3 (**Figure S3**a-c and **S4**a-c) and decreased with the increase of VO^{2+} concentration from 0.1 to 0.2 M (**Figure S3**c-e and **S4**a-c). The highest porosity of 58.3% is obtained in sample S3 (**Figure S3**f). Thus, the variation of porosity is negatively correlated with the VO^{2+} content in the precursor films. The particle diameter is essentially distributed around 80 nm (**Figure S3**f). And the slight decrease in diameter from sample S2 to S5 is almost negligible due to the statistical error.

According to our previous study that reveals the formation mechanism of highly dispersed VO_2 NPs by a similar solution method,[25] the porosity of the synthesized VO_2 film is significantly influenced by the solid content of VO^{2+} in the precursor film. The higher the VO_2 content, the lower the initial porosity. This is consistent with the porosity variation from samples S1 to S3 or samples S3 to S5. After removal of PVP, the densification process based on the sintering mechanism dominates the structural evolution. The particle diameter and shape are strongly dependent on the annealing temperature rather than the solid content of VO^{2+} in the precursor film. As can be seen, the diameter of VO_2 NPs (~82.8 nm) in samples S2-S5 prepared at 550 ºC is much smaller than that synthesized at 500 ºC (~126.6 nm).[25] Meanwhile, the densification process is accompanied by a decrease in the defect concentration, resulting in a significant improvement of the crystallinity of the VO_2 NPs.

2.2 Thermochromic Performance of the FDVP Film

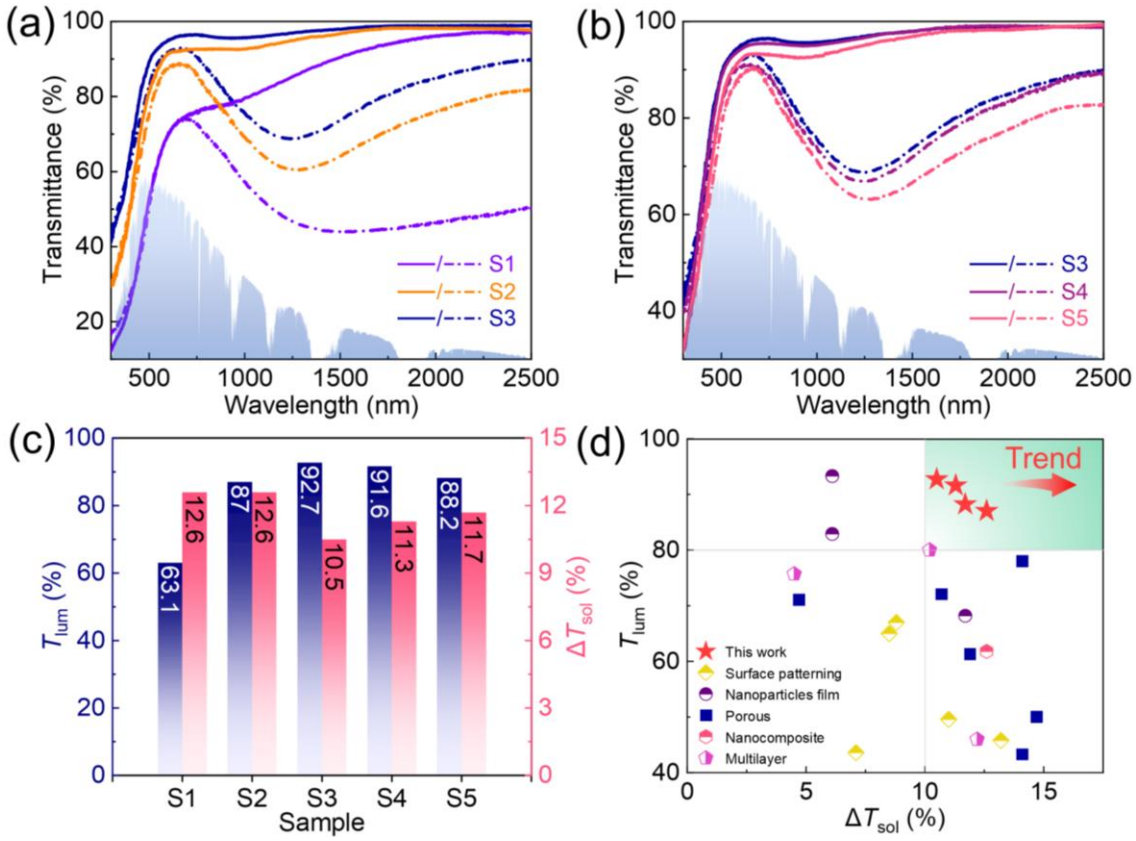

Figure 2 Transmittance of a) samples S1-S3 and b) samples S3-S5 (the solid line is tested at 30 ºC and the short dashed dotted line is tested at 100 ºC). c) T_{lum} and ΔT_{sol} of samples S1-S5. d) Comparison in optical performance between this work and some state-of-the-art works.

The typical characteristics such as ultra-high transparency, light tan color, small particle size, fully discrete and highly crystalline NPs of the FDVP film make it considerably promising for smart window applications according to previous works.[15,16,18,24,27] Therefore, the optical properties related to the smart window are investigated. **Figure 2**a,b show the transmittance of samples S1-S5 tested at 30 and 100 ºC. Samples S2-S5 with high porosity have the ultra-high transmittance of over 90% in the visible and NIR region at 30

ºC (VO_2(M)). At 100 ºC (VO_2(R)), a significant decrease in transmittance in the NIR region is observed due to the STM transition, and the largest loss is at around 1250 nm. Sample S1 has the relatively low visible transmittance and the maximum transmittance reduction is centered at 2500 nm. As shown in **Figure 3**c, the variation pattern of T_{lum} is consistent with that of porosity. In contrast, ΔT_{sol} shows the exact opposite variation pattern compared to T_{lum}, ΔT_{sol} and T_{lum} have a mutually antagonistic relationship. T_{lum} and ΔT_{sol} are both controllable by changing the synthesis conditions. The FDVP film with the highest porosity presents the optimum optical performance with T_{lum} of 92.7% and ΔT_{sol} of 10.5%. A good optical performance with T_{lum} of 91.6% and ΔT_{sol} of 11.3% is also obtained in sample S4. It is extremely valuable that such ultra-transparent VO_2 films simultaneously show ΔT_{sol} of over 10%. Additionally, although the first-order STM transition is accompanied by the crystal volume change, but no change in transmittance of the FDVP film after 100 cycles of STM transition is observed, which indicates that the firm adhesion between the VO_2 NPs and the quartz glass (**Figure S5**).

The comparisons in optical performance between the FDVP film and some state-of-the-art thermochromic VO_2 films have been made (**Figure 2**d and **Table S2**) to highlight its superiority. Lots of strategies regarding surface patterning,[15,21,24,28-30] nanoparticle films,[16,22,31] porous structures,[14,18,27,32-34] nanocomposite films,[35] and multilayer films[36-38] have been employed to improve ΔT_{sol} to more than 10%, but none of them can simultaneously achieve the T_{lum} above 90%. The surface patterning technique produces films with structure similar to the FDVP film, while most of them have poor performance.[21,24,28] To the best of our knowledge, the thermochromic performance of the FDVP film reaches a new milestone in the thermochromic VO_2 films for smart windows.

2.3 Origination of the Excellent Thermochromic Performance

In order to reveal the origination of the excellent thermochromic performance of the FDVP film, the FDTD simulations are performed on both the VO_2 particulate film and VO_2 continuous film (**Figure 3**d). As can be seen in the VO_2 particulate film, the confined electric field intensity around the VO_2(R) NPs (**Figure 3**b) is significantly enhanced compared to that around the VO_2(M) NPs (**Figure 3**a), indicating that the strong LSPR effect occurred between the electric field generated in the VO_2(R) NPs and the incident electromagnetic wave at the wavelength of 1330 nm. And the LSPR effect results in a remarkable absorption of NIR light by the VO_2(R) particulate film (**Figure 3**c). To specifically demonstrate the LSPR effect of the FDVP film, the temperature dependent transmittance (300-2500 nm) is measured from 30 to 100 ºC. The corresponding temperature dependent extinction (**Figure 3**d,e) is derived from the equation A = -lg(transmittance). As the temperature increases, the metallic VO_2(R) content is steadily increased, and the LSPR is switched on, resulting in the absorption intensity of NIR light by the VO_2(R) NPs increased. Conversely, as the temperature drops, the metallic VO_2(R) content is decreased and the LSPR is switched off. In the FDVP film, the LSPR effect is further enhanced by doubling the content of VO_2 NPs through the specially designed double-side structures, [31] and by increasing the crystallinity of VO_2 NPs through annealing at high temperature. Thus, an excellent ΔT_{sol} is achieved.

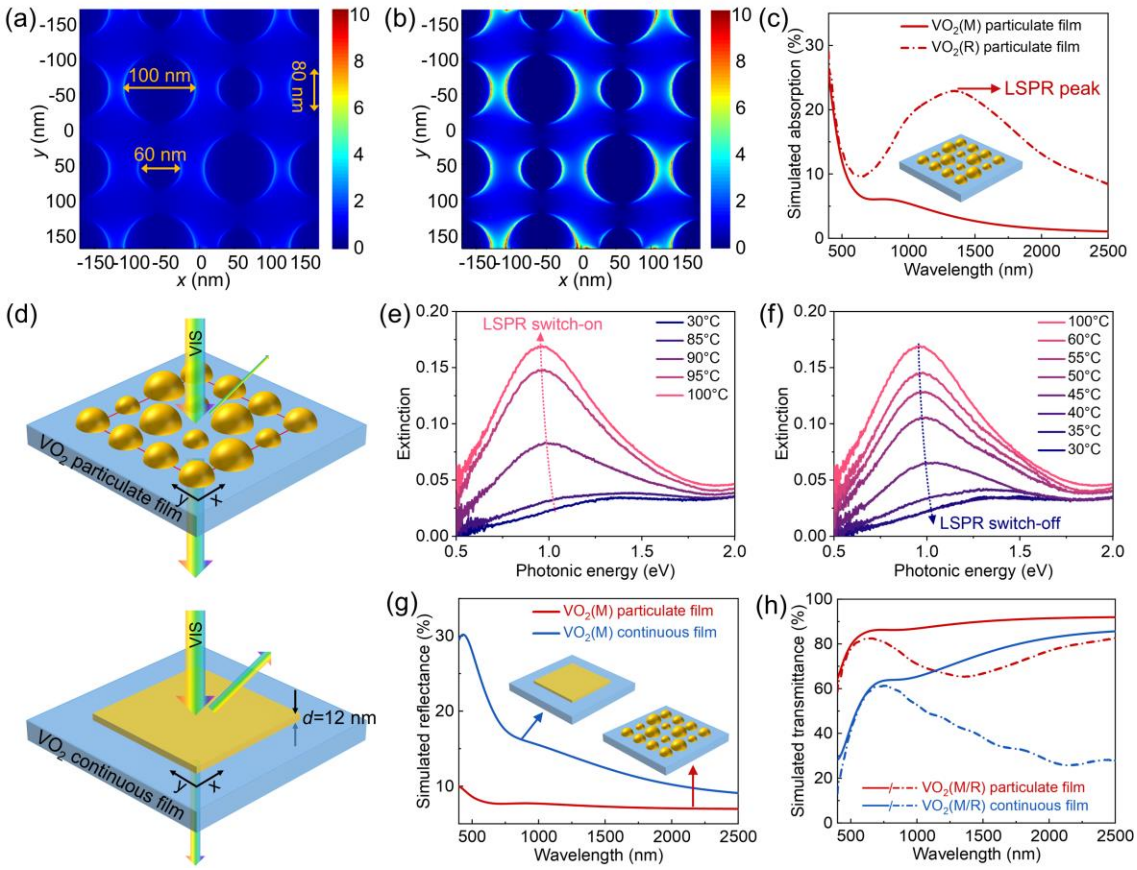

Figure 3 Simulated in-plane (x-y) electric fields of the a) VO_2(M) and b) VO_2(R) particulate films at wavelength of 1330 nm. c) Simulated absorption of the VO_2(M/R) particulate films. d) Structure configurations of the VO_2 particulate film and VO_2 continuous film for simulation, and the demonstration of different visible transmittance and reflectance of the films. Temperature dependent LSPR of the FDVP film during e) heating stage and f) cooling stage. Simulated g) reflectance and h) transmittance of the double-side VO_2 particulate film and double-side VO_2 continuous film.

ΔT_{sol} is generally positively related to the VO_2 content in the film, thus the optical properties of continuous and particulate films with the same VO_2 content are compared in the simulations. The reflectance in visible region of the VO_2 particulate film is significantly

reduced compared to that of the VO_2 continuous film (**Figure 3**g). As a result, T_{lum} derived from the simulated transmittance spectrum (**Figure 3**h) of the double-side VO_2 continuous film is only 51.1%, while it is increased to 82.1% for the VO_2 particulate film. Interestingly, the NIR light modulation of the continuous film appears to be larger, but the ΔT_{sol} of the particulate film is comparable to that of the continuous film because of the fact that the smaller the wavelength, the higher the solar energy. Meanwhile, n_{eff} of the VO_2 particulate film can be roughly calculated by the equation, $n_{eff} = f_{air} \cdot n_{air} + (1-f_{air}) \cdot n_{VO_2}$, where f_{air} is the film porosity. n_{eff} is decreased with the increase of porosity. For the FDVP film, it is estimated that a minimum n_{eff} of 1.75 at 550 nm could be obtained from the highest porosity of 58.3%. According to the Fresnel equation, $R=[(n_1-n_2)/(n_1+n_2)]^2$, where R is the interface reflectance, n_1 and n_2 denote the refractive index of two medium. Therefore, the total reflectance from the air/FDVP film interface and the FDVP film/quartz glass interface could be estimated to be about 8% at 550 nm (n_{air}=1, $n_{VO_{2(M)}}$=2.8), which is in good agreement with the measured transmittance regardless of the effect of film absorption at 550 nm. In addition, the estimated transmittances at 550 nm for other samples are also in good agreement with the measured results (**Figure S6**). However, the measured transmittance is much lower than the estimated one in sample S1. This may be ascribed to the visible light scattering from agglomerated VO_2 particles in sample S1 during the test, while the scattering effect is ignored in the estimated result. Apparently, in the discrete VO_2 particulate films, the light scattering is negligible, thus the estimated results are more consistent with the measured ones. According to above results, the ultra-high T_{lum} of FDVP film is mainly attributed to the reduced reflectance induced by the ultra-high porosity and the discrete VO_2 NPs with a diameter of around 82.6 nm.

2.4 Thermochromic Performance of the W Doped FDVP Film

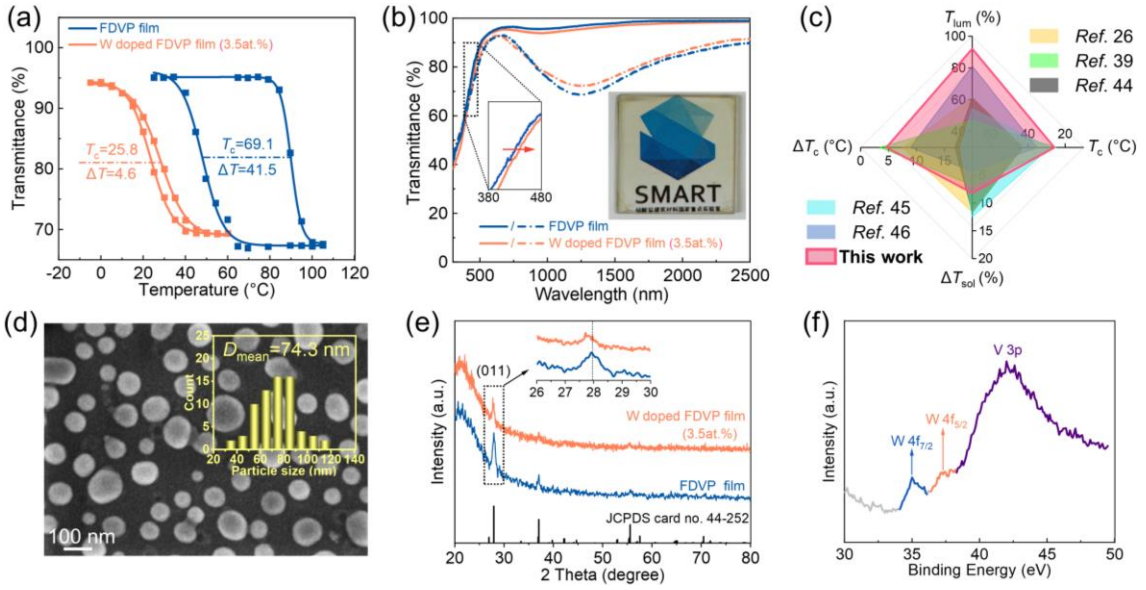

Figure 4 a) Thermal hysteresis loops of the FDVP film and the 3.5at.%W doped FDVP film, the square dots are the tested data, and the curves are obtained by *Boltzmann* fitting. b) Transmittance spectra of the FDVP film and the 3.5at.%W doped FDVP film, the inset shows the photograph of the ultra-transparent 3.5at.%W doped FDVP film. c) Comparison in comprehensive thermochromic properties between the 3.5at.% W doped FDVP film and some state-of-the-art VO_2 films with decreased T_c. d) SEM images of the 3.5at.%W doped FDVP film, the inset shows the histogram of the particle size distribution. e) XRD patterns of the FDVP film and the 3.5at.%W doped FDVP film. f) XPS result of the 3.5at.%W doped FDVP film.

It is crucial to reduce T_c of VO_2 films for smart windows application [17,39,40] According to the thermal hysteresis loop (**Figure 4**a), T_c and ΔT_c (difference between the phase transition temperatures in the heating and cooling stages) of the FDVP film are determined to be 69.1 and 41.5 ºC, respectively. It indicates the low defect concentration in the VO_2

NPs.[39,41,42] However, such high T_c and ΔT_c would undoubtedly hinder its practical application.

W doping is a very promising approach to reduce the T_c of VO_2 films[26,43,44] and is employed here to obtain high performance FDVP film with T_c at around room temperature (25 ºC). The XPS result (**Figure 4**f) confirms that W^{6+} exists in the 3.5at.%W doped FDVP film. No impurity corresponding to tungsten oxide is observed in the XRD pattern (**Figure 4**e), and the diffraction peak for the (011) plane shifts to a small angle due to the plane spacing increased. This indicates that lattice expansion is induced due to W^{6+} (radius of 0.6 nm) is successful replaces V^{4+} (radius of 0.58 nm) in the lattice.[26] The diffraction peak intensity of the (011) plane is decreased after W doping, revealing that the defect concentration is increased. **Figure 4**a shows the thermal hysteresis loop of the 3.5at.%W doped FDVP film. T_c is successfully reduced from 69.1 ºC to 25.8 ºC, and ΔT_c is remarkably reduced from 41.5 ºC to 4.6 ºC. The ΔT_c of the 3.5at.%W doped FDVP film is extremely narrow compared to most of the reported studies.[15,23,26,39,41,44-46] Notably, ΔT_c is a rarely noticed but key factor that determines the solar energy modulating ability of VO_2 films, and which is expected to be as low as possible.[41,47] The decrease in T_c is ascribed to the increased electron and defect concentration in the crystal induced by the substitution doping of W^{6+}, which accelerates the electronic and structural phase transitions, respectively.[17] The reduction in ΔT_c is attributed to the increased defect concentration, which enriches the activated defects for nucleation across the STM transition.[39] The optical performance of the FDVP film is also affected by W doping. As shown in **Figure 4**b, the LSPR effect intensity is reduced due to the crystallinity of W doped VO_2 NPs is decreased, resulting in a reduced ΔT_{sol} of 8.2%. Although, the increased electron

concentration in the 3.5at.%W doped FDVP film narrowed the band gap width and thus results in a red-shift of the absorption edge. But the T_{lum} of 92.0% is barely affected and the film is still ultra-transparent (the inset in **Figure 4**b), since the diameter of W doped VO_2 NPs is decreased to 74.3 nm (**Figure 4**d). As a result, the 3.5at.%W doped FDVP film delivers excellent thermochromic performance, and also outperforms the state-of-the-art VO_2 films with reduced T_c and ΔT_c (**Figure 4**c and **Table S3**). In most studies, VO_2 films with T_c at room temperature present unsatisfactory optical properties. To evaluate the stability of the 3.5at.%W doped FDVP film, we measure its transmittance after 280 days (**Figure S**7), the film is placed indoors and exposes to air. T_{lum} is almost unchanged, but ΔT_{sol} is decreased from 8.2% to 7.3%. It suggests that the stability is less than satisfactory, as the film has not yet really been subjected to harsh outdoor conditions. According to the previous reports focused on improving the environmental stability of VO_2 films, the addition of a transparent protective layer (SiO_2,[48] HfO_2,[49] ZnO[50] etc.) could effectively improve the stability. However, there should be a good refractive index fit between the FDVP film and the protective layer to avoid optical properties loss. This would be the focus of the subsequent work.

2.5 Demonstration of the Solar Energy Modulation of the FDVP Film

The solar energy modulating ability of the FDVP film is further evaluated by a homemade demonstration device (**Figure 5**a). The FDVP film and bare glass are used to prevent water from being heated by the NIR light. The temperatures of water (CH1) and FDVP film (or glass) (CH2) as a function of irradiation time are recorded in **Figure 5**b,c. The temperature of the water under the FDVP film is lower than the temperature of the water under the bare glass. The temperature difference of the water become more

pronounced as the irradiation time increased. The maximum value approaches to 3.4 ºC when the irradiation time is 20 minutes. Such a difference is impressive because water has a very limited absorption of NIR light. It demonstrates the excellent solar energy modulation ability of the FDVP film. The reduced solar energy is mainly absorbed by the FDVP film because the temperature of the FDVP film is almost 46 ºC higher than the temperature of the bare glass after the system is stabilized. This can only be attributed to the intense photothermal effect induced by the LSPR effect in the VO_2(R) NPs. It also indirectly proves the existence of the LSPR.

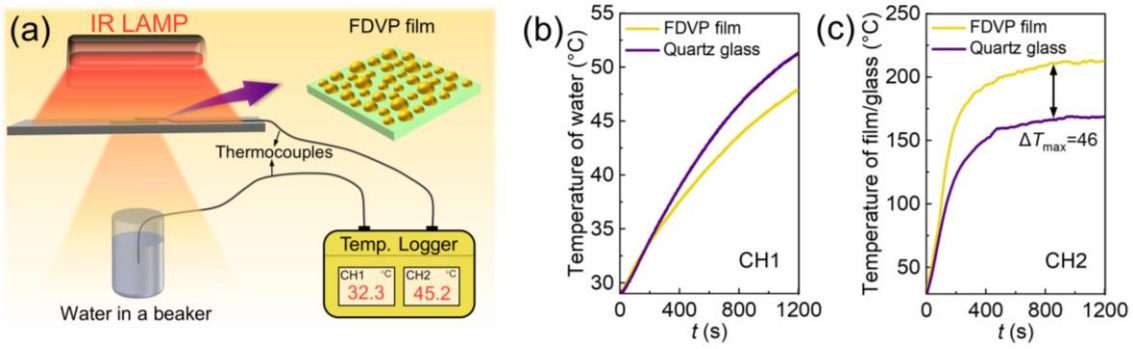

Figure 5 a) Schematic illustration of the demonstration of the solar energy modulation ability of FDVP film. b) Temperatures of the water in a beaker. c) Temperatures of the bare glass and the FDVP film.

3. Conclusion

In summary, we fabricate the FDVP films with VO_2 NPs randomly dispersed on both sides of the glass *via* a novel template-free solution method. The FDVP film is ultra-transparent with a T_{lum} of up to 92.7%. It also exhibits reversible switching between the NIR transparent state and the NIR blocking state across the STM transition, resulting in an excellent ΔT_{sol} of 10.5%. Such features make it promising for smart windows. The

origination of the superior thermochromic performance is theoretically revealed by the FDTD simulation. The ultra-high T_{lum} is attributed to the significantly reduced reflectance. The NIR light absorption of the LSPR effect in VO_2(R) NPs is responsible for the excellent ΔT_{sol}. Additionally, the T_c and ΔT_c of the FDVP film can be effectively reduced from 69.1 ºC and 41.5 ºC to 25.8 ºC and 4.6 ºC through doping with 3.5at.%W. And the 3.5at.%W doped FDVP film also shows excellent optical performance with T_{lum} of 92.0% and ΔT_{sol} of 8.2%. Thus, this work can promote the practical application of VO_2 in smart windows and open up opportunities for the development of ultra-transparent VO_2 films with good thermochromic performance for diverse applications.

4. Experimental Section

Materials: Vanadium pentoxide (V_2O_5, 99.5%, Aladdin), ammonium metatungstate ($H_{28}N_6O_{41}W_{12}$, 99.5%, Aladdin), polyvinylpyrrolidone (PVP, K88-96, Aladdin), oxalic acid dihydrate ($H_2C_2O_4 \cdot 2H_2O$, 99.7%, Sinopharm), and quartz glass (25*25*1 mm, Wenli Glass) were used as received.

Preparation of VOC_2O_4-PVP Solution: Typically, 0.045 mol of $H_2C_2O_4 \cdot 2H_2O$ and 0.015 mol of V_2O_5 were added to 100 mL of deionized water, and the solution was stirred at 80 ºC until a clear blue VOC_2O_4 solution (0.3 M) was obtained. The solution concentration was diluted with excess deionized water to 0.1 M, 0.15 M and 0.2 M, respectively. Different amounts of PVP as the film forming agent were then added to the above solutions under vigorous stirring. The content of PVP in the final VOC_2O_4/PVP solutions was 6 wt%.

Fabrication of VO_2 Films: First, quartz glass substrates were cleaned in acetone, deionized water, and ethanol under ultrasonication for 30 min successively. VOC_2O_4/PVP

solutions with different concentrations of 0.1 M, 0.15 M and 0.2 M were spin-coated on both sides of the substrate respectively to form different precursor films. In detail, the VOC_2O_4/PVP solution was dropped onto the substrate followed by spin-coating at 500 rpm for 5 s and 3000 rpm for 25 s. To investigate the effect of the thickness of precursor films on the structures of VO_2 films, the 0.1 M of VOC_2O_4/PVP solution was also spin-coated on the substrate at 500 rpm for 5 s and 2000 rpm for 25 s, 500 rpm for 5 s and 1000 rpm for 25 s respectively. After drying the single-side VOC_2O_4/PVP precursor film at 80 ºC for 20 min, VOC_2O_4/PVP solutions were also spin-coated on the other side of the substrate under the same conditions (solution concentration and spin-coating process). The double-side VOC_2O_4/PVP precursor films were converted into VO_2 films by annealing in a tube furnace at 550 ºC for 1 h. A suitable amount of air was left in the tube furnace. The certain amount of O_2 in the tube furnace was necessary to completely remove the PVP and promote the structure evolutions according to our previous study.[25] The W doped FDVP film was prepared under the same conditions as sample S3 (FDVP film), except that a certain amount of ammonium metatungstate was added to the 0.1 M VOC_2O_4/PVP solution (molar ratio of W to V was 3.5%).

Characterizations: The crystal structure of the FDVP film was determined by a grazing incidence angle X-ray diffractometer (GIXRD, Empyrean), the radiation source was Cu Kα, the scan range was 10 to 80°, the scan rate was 5°/min. A Raman spectrometer (inVia, Renishaw) with an excitation source from 633 nm laser was also used to test the composition of the FDVP film. The valence state of the elements in the FDVP film was characterized by a X-ray photoelectron spectrometer (XPS, ESCALAB 250Xi, ThermoFisher). A Field emission scanning electron microscope (FE-SEM, Zeiss Ultra

Plus) and an atomic force microscopy (AFM, Bruker Dimension ICON) were employed to observe the morphologies of top surface of the VO_2 films. An UV-vis-NIR spectrophotometer (UV-3600, SHIMADZU) with a temperature controller was adopted to test the temperature dependent transmittance (300-2500 nm) of VO_2 films (tested at 30 ºC and 100 ºC) and the 3.5at.%W doped FDVP film (tested at 0 ºC and 60 ºC), respectively. Thermal hysteresis loops were plotted based on the transmittance at a given wavelength, the transmittance was tested at each 5 ºC variation in film temperatures during the heating and cooling stages. T_c and ΔT_c were determined from the thermal hysteresis loops. T_{lum} (380-780 nm) and solar energy transmittance (T_{sol}, 300-2500 nm) were derived from equations (1),

$$T_{lum/sol} = \int \delta_{lum/sol}(\lambda) T(\lambda) d\lambda / \int \delta_{lum/sol}(\lambda) d\lambda \quad (1)$$

where $T(\lambda)$ is the transmittance, $\delta_{lum}(\lambda)$ is the spectral luminous efficiency function for photopic vision, the $AM_{1.5}$ solar spectral irradiance is denoted as $\delta_{sol}(\lambda)$.[25] ΔT_{sol} was determined by $\Delta T_{sol} = T_{sol}$ (M phase) - T_{sol} (R phase).

Simulations: The Finite Difference Time Domain (FDTD) method was used to simulate the optical properties of the VO_2 particulate film and the VO_2 continuous film. Due to the VO_2 NPs were polydisperse in the SEM results, the VO_2 NPs in the particulate film model were treated as a periodic array of hemispheres with diameters of 60, 80 and 100 nm, respectively. The porosity was 58.3%, that was the same as sample S3. For comparison, the VO_2 volume of the continuous film was the same as that of the particulate film, so the thickness of the continuous film was determined to be 12 nm. The detailed configurations of the film structures are shown in Figure 3c. The optical constants (n, k) of VO_2(M) and

VO_2(R) were taken from the previous work.[51] A plain wave (400-2500 nm) was injected from the top surface of the VO_2 films. Only the transmittance (T_s) and reflectance (R_s) of a single-sided film were simulated, and the transmittance (T_d) and reflectance (R_d) of a double-sided film can be estimated as T_s^2 and $T_s \times R_s + R_s$, respectively. The simulated absorption was derived from 1- T_d- R_d.

Demonstration of Solar Energy Modulation: In the demonstration experiment, a 1000 W NIR lamp (LANGPRO Lightsources, R10-395-2000) was served as the solar light source. A thermal baffle (20 mm in thickness) with a 20*20 mm^2 glass window was right below the NIR lamp. In the test, the glass window was covered by a 25*25 mm^2 bare glass or the FDVP film. And 20 ml of deionized water in a 100 ml beaker was right below the glass window. The distance from the lamp to the glass window and from the glass window to the water surface was 10 cm and 30 cm, respectively. Two T-type thermocouples were placed in the water and on the surface of the bare glass or the FDVP film, and the temperatures were recorded per second by the temperature logger.

Acknowledgements

This work was supported by the National Natural Science Foundation of China (Grant No. 51772229 and 52062045), the 111 project (No. B18038), the National Key R&D Program of China (No. 2017YFE0192600), Key R&D Project of Hubei Province (No.2020BAB061), National innovation and entrepreneurship training program for college students (No. 201910497034), Open Foundation of the State Key Laboratory of Silicate Materials for Architectures at WUT (No. SYSJJ2020-04), State Key Laboratory of Materials Processing and Die & Mould Technology, Huazhong University of Science and

Technology (No. P2021-010) and the Fundamental Research Funds for the Central Universities (No. 195201024). We also thank the Analytical and Testing Center of WUT for the help with carrying out the materials characterization.

Conflict of Interest

The authors declare no conflict of interest.

References

[1] Y. Ke, S. Wang, G. Liu, M. Li, T. J. White, Y. Long, *Small* **2018**, 14, e1802025.

[2] F. J. Morin, *Phys. Rev. Lett*. **1959**, 3, 34-36.

[3] S. C. Wang, T. Y. Jiang, Y. Meng, R. G. Yang, G. Tang, Y, Long, *Science* **2021**, 374, 1501-1504.

[4] K. Sun, W. Xiao, C. Wheeler, M. Simeoni, A. Urbani, M. Gaspari, S. Mengali, C. H. de Groot, O. L. Muskens, *Nanophotonics* **2022**, 11, 4101.

[5] B. Wu, D. Zhang, C.-H. Wang, K. Zhang, X. Wu, *Phys. Chem. Chem. Phys.* **2023**.

[6] R. Beaini, B. Baloukas, S. Loquai, J. E. Klemberg-Sapieha, L. Martinu, *Sol. Energy Mater. Sol. Cells* **2020**, 205, 110206.

[7] A. Tripathi, J. John, S. Kruk, Z. Zhang, H. S. Nguyen, L. Berguiga, P. R. Romeo, R. Orobtchouk, S. Ramanathan, Y. Kivshar, S. Cueff, *ACS Photonics* **2021**, 8, 1206.

[8] S. Chandra, D. Franklin, J. Cozart, A. Safaei, D. Chanda, *ACS Photonics* **2018**, 5, 4513;

[9] L. Xiao, H. Ma, J. Liu, W. Zhao, Y. Jia, Q. Zhao, K. Liu, Y. Wu, Y. Wei, S. Fan, K. Jiang, *Nano Lett.* **2015**, 15, 8365.

[10] Z. Lu, Y. Zhang, H. Wang, C. Xia, Y. Liu, S. Dou, Y. Li, J. Tan, *Engineering* **2022**, in press. doi.org/10.1016/j.eng.2022.10.005

[11] G. Liu, S. Wang, A. I. Y. Tok, T. J. White, C. Li, M. Layani, S. Magdassi, M. Li, Y. Long, *ACS Omega* **2019**, 4, 19635.

[12] K. Liu, S. Lee, S. Yang, O. Delaire, J. Wu, *Mater. Today* **2018**, 21, 875.

[13] X. Li, C. Cao, C. Liu, W. He, K. Wu, Y. Wang, B. Xu, Z. Tian, E. Song, J. Cui, G. Huang, C. Zheng, Z. Di, X. Cao, Y. Mei, *Nat. Commun.* **2022**, 13, 7819.

[14] S. Long, X. Cao, R. Huang, F. Xu, N. Li, A. Huang, G. Sun, S. Bao, H. Luo, P. Jin, *ACS Appl. Mater. Interfaces* **2019**, 11, 22692-22702.

[15] M. Liu, B. Su, Y. V. Kaneti, Z. Chen, Y. Tang, Y. Yuan, Y. Gao, L. Jiang, X. Jiang, A. Yu, *ACS Nano* **2017**, 11, 407-415.

[16] Y.-C. Lu, C.-H. Hsueh, *ACS Appl. Nano Materials* **2022**, 5, 2923-2934.

[17] Y. Cui, Y. Ke, C. Liu, Z. Chen, N. Wang, L. Zhang, Y. Zhou, S. Wang, Y. Gao, Y. Long, *Joule* **2018**, 2, 1-40.

[18] L. Kang, Y. Gao, H. Luo, Z. Chen, J. Du, Z. Zhang, *ACS Appl. Mater. Interfaces* **2011**, 3, 135-138.

[19] M. Aburas, V. Soebarto, T. Williamson, R. Liang, H. Ebendorff-Heidepriem, Y. Wu, *Appl. Energy* **2019**, 255.

[20] R. Sun, B. Jin, L. Yao, Y. Liu, J. Li, J. Liang, J. He, *ACS Appl. Mater. Interfaces* **2021**, 13, 13751-13759.

[21] Q. Lu, C. Liu, N. Wang, S. Magdassi, D. Mandler, Y. Long, *J. Mater. Chem. C* **2016**, 4, 8385-8391.

[22] C. Geng, S. Dou, J. Zhao, F. Ren, J. Gu, H. Wei, H. Guan, S. Liang, L. Li, Y. Li, Z. Tian, *Appl. Surf. Sci.* **2022**, 592, 153267.

[23] J. Zhu, Y. Zhou, B. Wang, J. Zheng, S. Ji, H. Yao, H. Luo, P. Jin, *ACS Appl. Mater. Interfaces* **2015**, 7, 27796-27803.

[24] Y. Ke, X. Wen, D. Zhao, R. Che, Q. Xiong, Y. Long, *ACS Nano* **2017**, 11, 7542-7551.

[25] B. Li, S. Tian, J. Qian, S. Wu, B. Liu, X. Zhao, *Ceram. Int.* **2023**, 49, 2310-2318.

[26] B. Li, S. Tian, H. Tao, X. Zhao, *Ceram. Int.* **2019**, 45, 4342-4350.

[27] S. Long, X. Cao, Y. Wang, T. Chang, N. Li, L. Jin, L. Ma, F. Xu, G. Sun, P. Jin, *Sol. Energy Mater. Sol. Cells* **2020**, 209, 110449.

[28] X. Qian, N. Wang, Y. Li, J. Zhang, Z. Xu, Y. Long, *Langmuir* **2014**, 30, 10766-10771.

[29] N. Wang, Y. K. Peh, S. Magdassi, Y. Long, *J. Colloid Interf. Sci.* **2018**, 512, 529-535.

[30] Y. Ke, I. Balin, N. Wang, Q. Lu, A. I. Tok, T. J. White, S. Magdassi, I. Abdulhalim, Y. Long, *ACS Appl. Mater. Interfaces* **2016**, 8, 33112-33120.

[31] S. Dou, J. Zhao, W. Zhang, H. Zhao, F. Ren, L. Zhang, X. Chen, Y. Zhan, Y. Li, *ACS Appl. Mater. Interfaces* **2020**, 12, 7302-7309.

[32] Z. Wang, B. Li, S. Tian, B. Liu, X. Zhao, X. Zhou, G. Tang, A. Pang, *Materials (Basel)* **2021**, 14, 4927.

[33] B. Zhuang, Z. Dai, S. Pang, H. Xu, L. Sun, F. Ma, *Adv. Opt. Mater.* **2019**, 7.

[34] X. Cao, N. Wang, J. Y. Law, S. C. Loo, S. Magdassi, Y. Long, *Langmuir* **2014**, 30, 1710-1715.

[35] Z. Qu, L. Yao, J. Li, J. He, J. Mi, S. Ma, S. Tang, L. Feng, *ACS Appl. Mater. Interfaces* **2019**, 11, 15960-15968.

[36] H. Guo, Y. G. Wang, H. R. Fu, A. Jain, F. G. Chen, *Sol. Energy Mater. Sol. Cells* **2020**, 211, 110528.

[37] J. Zhang, J. Wang, C. Yang, H. Jia, X. Cui, S. Zhao, Y. Xu, *Sol. Energy Mater. Sol. Cells* **2017**, 162, 134.

[38] T. Chang, X. Cao, N. Li, S. Long, X. Gao, L. R. Dedon, G. Sun, H. Luo, P. Jin, *ACS Appl. Mater. Interfaces* **2017**, 9, 26029-26037.

[39] B. Li, S. Tian, Z. Wang, B. Liu, X. Gong, X. Zhao, *Appl. Surf. Sci.* **2021**, 568, 150959.

[40] Y. Xue, S. Yin, *Nanoscale* **2022**, 14, 11054-11097.

[41] J. Schläefer, C. Sol, T. Li, D. Malarde, M. Portnoi, T. J. Macdonald, S. K. Laney, M. J. Powell, I. Top, I. P. Parkin, I. Papakonstantinou, *Sol. Energy Mater. Sol. Cells* **2019**, 200, 109944.

[42] R. Lopez, T. E. Haynes, L. A. Boatner, L. C. Feldman, R. F. Haglund, *Phys. Rev. B* **2002**, 65, 224113.

[43] D. Kolenaty, J. Vlcek, T. Barta, J. Rezek, J. Houska, S. Haviar, *Sci Rep* **2020**, 10, 11107.

[44] L. Zhang, F. Xia, J. Yao, T. Zhu, H. Xia, G. Yang, B. Liu, Y. Gao, *J. Mater. Chem. C* **2020**, 8, 13396-13404.

[45] Q. Zhou, W. Lv, Q. Qiu, T. Zhou, C. Huang, L. Li, *Ceram. Int.* **2020**, 46, 4786-4794.

[46] N. Wang, S. Liu, X. T. Zeng, S. Magdassi, Y. Long, *J. Mater. Chem. C* **2015**, 3, 6771-6777.

[47] M. E. A. Warwick, I. Ridley, R. Binions, *Sol. Energy Mater. Sol. Cells* **2015**, 140, 253-265.

[48] T. Chang, X. Cao, L.R. Dedon, S. Long, A. Huang, Z. Shao, N. Li, H. Luo, P. Jin, *Nano Energy* **2018**, 44, 256-264.

[49] T. Chang, X. Cao, N. Li, S. Long, Y. Zhu, J. Huang, H. Luo, P. Jin, *Matter* **2019**, 1, 734-744.

[50] Y. Chen, X. Zeng, J. Zhu, R. Li, H. Yao, X. Cao, S. Ji, P. Jin, *ACS Appl. Mater. Interfaces* **2017**, 9, 27784-27791.

[51] S. Y. Li, G. A. Niklasson, C. G. Granqvist, *J. Appl. Phys.* **2010**, 108. 063525.